ADVANCED FUNCTIONAL MATERIALS
www.afm-journal.de

Electrochemical Nitrate Reduction to Ammonia on CuCo Nanowires at Practical Level

Kouer Zhang, Pengting Sun, Yulun Huang, Mingcong Tang, Xiaohong Zou, Zhefei Pan, Xiaoyu Huo, Jie Wu, Chunche Lin, Zhongti Sun, Yangyang Wan, Xiao Zhang,* and Liang An**

Electrochemical reduction of nitrate (NO_3RR) holds great promise for environmentally friendly ammonia production. Tandem catalysis is a promising strategy for boosting the NO_3RR and inhibiting side effects, but it is still challenged by lacking well-designed catalysts to drive this catalytic process. Herein, the study develops the CuCo branched nanowires (CuCo NW) catalyst, which efficiently converts NO_3^- to NH_3 on Co (111) and Cu (111) crystal facets through a tandem catalysis mechanism. The in situ grown CuCo NW on Cu foam demonstrates a remarkable Faraday efficiency of 90.3% at 1.0 A cm^{-2} and maintains stable operation for 200 h at 100 and 200 mA cm^{-2} in a flow reactor. Density functional theory calculations suggest that the initial absorption and subsequent deoxygenation of $*NO_3$ on Co (111) leading to the formation of $*NO_2$, followed by its transfer to Cu (111) and further conversion to $*NH_3$, establish an optimal pathway by managing rate-determining steps on individual surfaces for NO_3RR. To showcase the practical application of the catalyst, the study further develops a scaling-up prototype reactor for continuous ammonia production, realizing the gram-level yield rate of 1474.09 mg h^{-1} and Faraday efficiency of 91.26% at practical-level 20.0 A.

1. Introduction

In recent years, the electrochemical conversion of nitrate to ammonia has emerged as a promising "green" alternative to the Haber–Bosch process for ammonia production. This approach offers the potential for a zero-carbon process, which could be powered by sustainable energy sources under ambient conditions.[1–4] Meanwhile, as a ubiquitous pollutant from industrial and agricultural activities, nitrate could cause severe eutrophication of water bodies and algal boom, threatening the balance of N-cycle.[5,6] In this context, the conversion of harmful nitrate to valuable ammonia utilizing carbon-free electricity exemplifies the concept of sustainable development. Generally, nitrate reduction reaction (NO_3RR) is directed as a half-cell reaction and written as the equation below:[7]

K. Zhang, M. Tang, X. Zou, X. Huo, J. Wu, X. Zhang, L. An
Department of Mechanical Engineering
The Hong Kong Polytechnic University
Hung Hom, Kowloon, Hong Kong SAR 999077, China
E-mail: xiao1.zhang@polyu.edu.hk; liang.an@polyu.edu.hk

P. Sun, Z. Sun, Y. Wan
Institute for Advanced Materials
School of Materials Science and Engineering
Jiangsu University
Zhenjiang, Jiangsu 212013, China
E-mail: yangyang.wan@ujs.edu.cn

The ORCID identification number(s) for the author(s) of this article can be found under https://doi.org/10.1002/adfm.202405179

© 2024 The Author(s). Advanced Functional Materials published by Wiley-VCH GmbH. This is an open access article under the terms of the Creative Commons Attribution-NonCommercial-NoDerivs License, which permits use and distribution in any medium, provided the original work is properly cited, the use is non-commercial and no modifications or adaptations are made.

DOI: 10.1002/adfm.202405179

Y. Huang, C. Lin
Institute of Organic and Polymeric Materials
National Taipei University of Technology
Taipei 106, Taiwan

Z. Pan
Key Laboratory of Low-grade Energy Utilization Technologies and Systems (Chongqing University)
Ministry of Education of China
Chongqing University
Chongqing 400044, China

Z. Pan
Institute of Engineering Thermophysics
School of Energy and Power Engineering
Chongqing University
Chongqing 400044, China

L. An
Research Institute for Smart Energy
The Hong Kong Polytechnic University
Hung Hom, Kowloon, Hong Kong SAR 999077, China

16163028, 2024, 44, Downloaded from https://onlinelibrary.wiley.com/doi/10.1002/adfm.202405179 by HONG KONG POLYTECHNIC UNIVERSITY HU NG HOM, Wiley Online Library on [03/11/2024]. See the Terms and Conditions (https://onlinelibrary.wiley.com/terms-and-conditions) on Wiley Online Library for rules of use; OA articles are governed by the applicable Creative Commons License

$$NO_3^- + 6H_2O + 8e^- \rightarrow NH_3 + 9OH^-$$
$$E_0 = 0.69 \text{ V vs. RHE} \quad (1)$$

The electrochemical reduction of nitrate to ammonia constitutes a complex process involving numerous electrochemical steps, resulting in the formation of various intermediates and potential side products, including N_2, NO, and N_2O.[8,9] In addition, a significant challenge confronting this process is the presence of the competing hydrogen evolution reaction (HER). Considering the theoretical onset potential of HER, the hydrogen evolution becomes increasingly favorable at more negative applied potentials, thereby impeding the rate of ammonia production through NO_3RR. Hence, the advancement of highly efficient catalysts is crucial to direct the reduction pathway toward the selective synthesis of ammonia.

Cu and Cu-based catalysts stand out among the transition-metal catalysts and are widely investigated in NO_3RR due to the similar energy levels of d-orbital of Cu and LUMO π^* (least unoccupied molecular orbital) of nitrate and relatively low HER activity.[8,10–12] However, due to the relatively poor *H supply, pure Cu catalysts usually encounter a significant uphill energy barrier during the hydrogenation process from nitrate to nitrite ($*NO_3 \rightarrow *NO_3H \rightarrow *NO_2$), serving as the rate-determining step (RDS) in NO_3RR[13] This hurdle directly impacts the reaction rate at the RDS, which is key to the development of efficient electrocatalysts. Therefore, it has been proposed to facilitate a synergy effect on Cu-based catalysts through alloying, fabricating core-shell structures, and implementation of tandem mechanisms, etc., to boost the NO_3RR performance.[14–21]

Nevertheless, given the complexity of electron transfer and the diversity of intermediates, it is difficult to find an optimum phase for all catalytic steps in NO_3RR due to the scaling relationship.[13,22,23] Motivated by the denitrification process of microorganisms, tandem catalysis decoupling the complicated 8-electron electrochemical process into individual steps on different catalysts/phases, providing alternative strategies to achieve full-step optimization of NO_3RR.[17,24,25] Recently, the tandem interaction of Cu (111) and Cu (100) facets is reported to attribute the high performance of NO_3RR, where NO_2^- generated on the Cu (100) facets is subsequently hydrogenated on the Cu (111) facets, solving this obstacle in sluggish hydrogenation of *NO to *NOH while mitigate the large energy barrier of $*NO_3$ to $*NO_2$ by Cu (111).[11] Moreover, He et al. first shed light on the possibility of tandem electrochemical nitrate reduction on Cu species and Co species,[17] while the specific reaction pathways/active sites are not clear enough and require further discussions. Notably, the intrinsic nature of Co facilitates the enhanced adsorption of *H species due to the more oxyphilic and less electronegative character, providing potential solutions for the RDS.[26] Therefore, we hypothesize that the combination of metallic Cu with Co capable of efficient nitrate deoxygenation shows promise in establishing an optimal pathway for NO_3RR through reducing the Gibbs free energies of RDS on each individual surface, thereby facilitating efficient nitrate-to-ammonia conversion.

Herein, we developed a tandem reaction strategy for NO_3RR to ammonia on Co (111) and Cu (111) by preparing CuCo branched nanowires on Cu foam (CuCo NW/Cu foam) (**Figure 1**a,b). As a result, the CuCo NW/Cu foam delivers the FE of 91.3% at the current density of 300 mA cm^{-2}, with an ammonia yield rate of 1.28 mmol h^{-1} cm^{-2} when operated in low nitrate concentration of 2000 ppm (0.032 M) of a static H-cell system, indicating the high intrinsic activity and selectivity of the catalyst. The density functional theory (DFT) study verifies the feasibility of the tandem catalysis mechanism and elucidates this process, where the Co (111) is favorable for nitrate conversion to nitrite, followed by the further deoxygenation and hydrogenation steps on Cu (111). More importantly, aiming at practical ammonia production, the as-prepared CuCo NW/Cu foam is applied as the cathode in the flow reactor and delivers the FE of 90.3% at 1.0 A cm^{-2} with enhanced mass transfer (Figure 1c). In our scaling-up prototype, a gram-level ammonia yield rate of 1.45 g h^{-1} is realized at the current of 20.0 A.

2. Results and Discussion

2.1. Catalyst Characterization

The CuCo NW catalyst is synthesized through in situ growth on Cu foam and hydrogen reduction to form the integrated electrode (Figure S1, Supporting Information). Besides, Cu NW and Cu-CoO NW are prepared as control groups through similar methods and characterized as well to compare NO_3RR performance. The details of the synthesis procedure are presented in the Supporting Information. Scanning electron microscopy (SEM) images present the morphology differences between the target catalyst and the control samples (Figure S2, Supporting Information). For Cu NW, nanowires with a diameter of 200 nm could be observed uniformly distributed on the surface of Cu foam. In comparison, CuCo NW presents with the branched nanowires structure (**Figure 2**a; Figure S3, Supporting Information), which brings about a larger surface area characterized through the calculation of electrochemical active surface area (ECSA) (Figure S6, Supporting Information). The twofold increasement in ECSA (from 9.32 to 16.03 mF cm^{-2}) of CuCo NW contributes to the exposure of more active sites for the reaction. High-resolution transmission electron microscopy (HRTEM) image indicates the presence of metallic Cu and Co in the CuCo NW due to the hydrogen reduction process during the synthesis, with a lattice spacing of 0.208 and 0.216 nm, corresponding to Cu (111) and Co (111), respectively (Figure 2b; Figure S4a, Supporting Information). The composition of the polycrystal in CuCo NW was confirmed by the appearance of a series of concentric rings in the selected area electron diffraction (SAED) pattern (Figure S4b, Supporting Information). The result of SAED is in accordance with the HRTEM while Cu (111) and Co (111) could be observed, respectively. Considering the stepwise growth of copper and cobalt, metallic Cu and Co exist in separate phases, rather than CuCo alloy, which is different from the former reported CuCo (111)[26] Besides, the corresponding X-ray diffraction (XRD) spectra for the whole electrode and the CuCo NW powder are shown in Figure S7 (Supporting Information).

The presence of active sites on the catalyst surface is essential for facilitating electrochemical reactions. Therefore, the X-ray photoelectron spectroscopy (XPS) analysis was applied to reveal the surface elemental states and composition of CuCo NW. The full XPS survey spectrum reveals the coexistence of Cu, Co, and O in the synthesized CuCo NW (Figure S30, Supporting

© 2024 The Author(s). Advanced Functional Materials published by Wiley-VCH GmbH
RIGHTSLINK

16163028, 2024, 44, Downloaded from https://onlinelibrary.wiley.com/doi/10.1002/adfm.202405179 by HONG KONG POLYTECHNIC UNIVERSITY HU NG HOM, Wiley Online Library on [03/11/2024]. See the Terms and Conditions (https://onlinelibrary.wiley.com/terms-and-conditions) on Wiley Online Library for rules of use; OA articles are governed by the applicable Creative Commons License

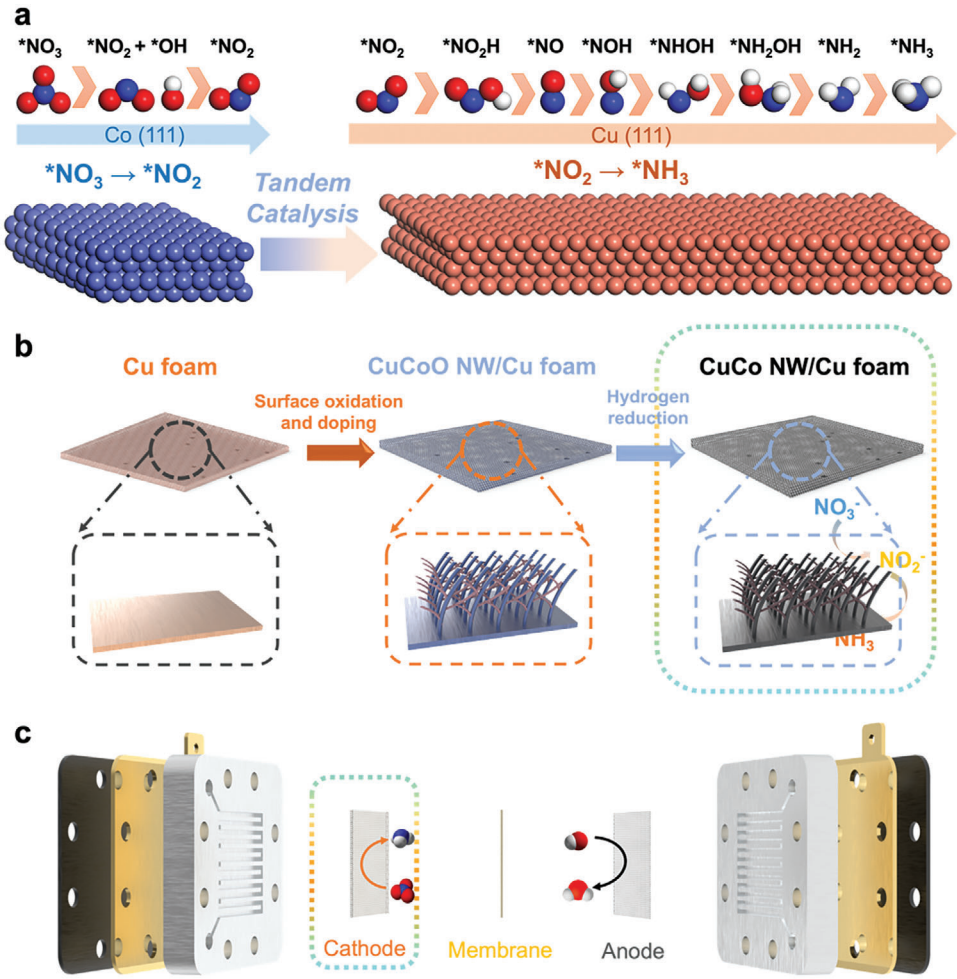

Figure 1. Schematic illustration for the enhancement of ammonia production performance. a) Tandem catalysis mechanism of Co (111) and Cu (111) facets. b) Synthesis process of CuCo NW/Cu foam. c) Fabrication of a scaling-up prototype.

Information). Notably, the comparison between CuCoO NW and CuCo NW is included to prove the formation of metallic Cu and Co during the hydrogen reduction process. As shown in the high-resolution XPS spectra of Cu 2p (Figure 2c), the peaks for CuO are located at 934.2 eV (Cu^{2+} $2p_{3/2}$) and 954.2 eV (Cu^{2+} $2p_{1/2}$), along with the shake-up satellite peaks in both the samples. Compared with the Cu 2p spectra of CuCoO NW, Cu^0 peaks appear at 932.4 eV (Cu^0 $2p_{3/2}$) and 952.3 eV (Cu^0 $2p_{1/2}$) in CuCo NW after the hydrogen reduction process.[26,27] To be mentioned, the Cu LMM spectrum indicates that the Cu element mainly exists in Cu^0 rather than Cu^+ (Figure S8, Supporting Information). In the XPS spectra of Co 2p (Figure 2d), the Co element is in the oxidation state of Co^{2+} before reduction, with the characteristic peaks at 780.7 eV (Co^{2+} $2p_{3/2}$) and 796.7 eV (Co^{2+} $2p_{1/2}$). However, after the hydrogen reduction process, the peaks for Co^0 appear at 776.7 eV (Co^0 $2p_{3/2}$) and 791.7 eV (Co^0 $2p_{1/2}$), which implies the surface CoO has been partially reduced in the synthesis process of CuCo NW. The Co $2p_{1/2}$-Co $2p_{3/2}$ spin-orbital splitting is ≈16 eV, which complies with previous reports.[28,29] According to the elemental ratio analysis provided by XPS (Table S2, Supporting Information), the ratio of Cu:Co is ≈2:1 on the surface of CuCo NW.

The energy dispersive spectroscopic (EDS) mapping revealed a uniform distribution of Cu and Co elements on the nanowire (Figure 2f; Figure S5 and Table S1, Supporting Information). Notably, through the image of elemental linear-scan analysis (Figure 2g) coupled with dark-field TEM, Co element distributes uniformly along the radial direction where the distribution of Cu element tends to be more concentrated in the center of the nanowire structure.

To achieve more accurate speciation of the catalyst composition, X-ray absorption spectroscopy (XAS) was applied to provide valuable information of the sample such as oxidation states, bond lengths, local geometry, coordination numbers, etc. For the K-edge X-ray absorption near-edge spectroscopy (XANES) of Cu and Co (Figure S9, Supporting Information), linear combination fitting is applied as well to figure out the composition and its corresponding ratio (Figure 2h,i). The results indicate that the composition of metallic Cu amounts to 43.3% while metallic Co amounts to 19.3% (Table S5, Supporting Information). In contrast, the component CuCoO NW without hydrogen reduction is 100% CuO and CoO. The results of linear combination fitting clearly demonstrated the decrease in the proportion of metal oxides during the hydrogen reduction process. The corresponding

© 2024 The Author(s). Advanced Functional Materials published by Wiley-VCH GmbH

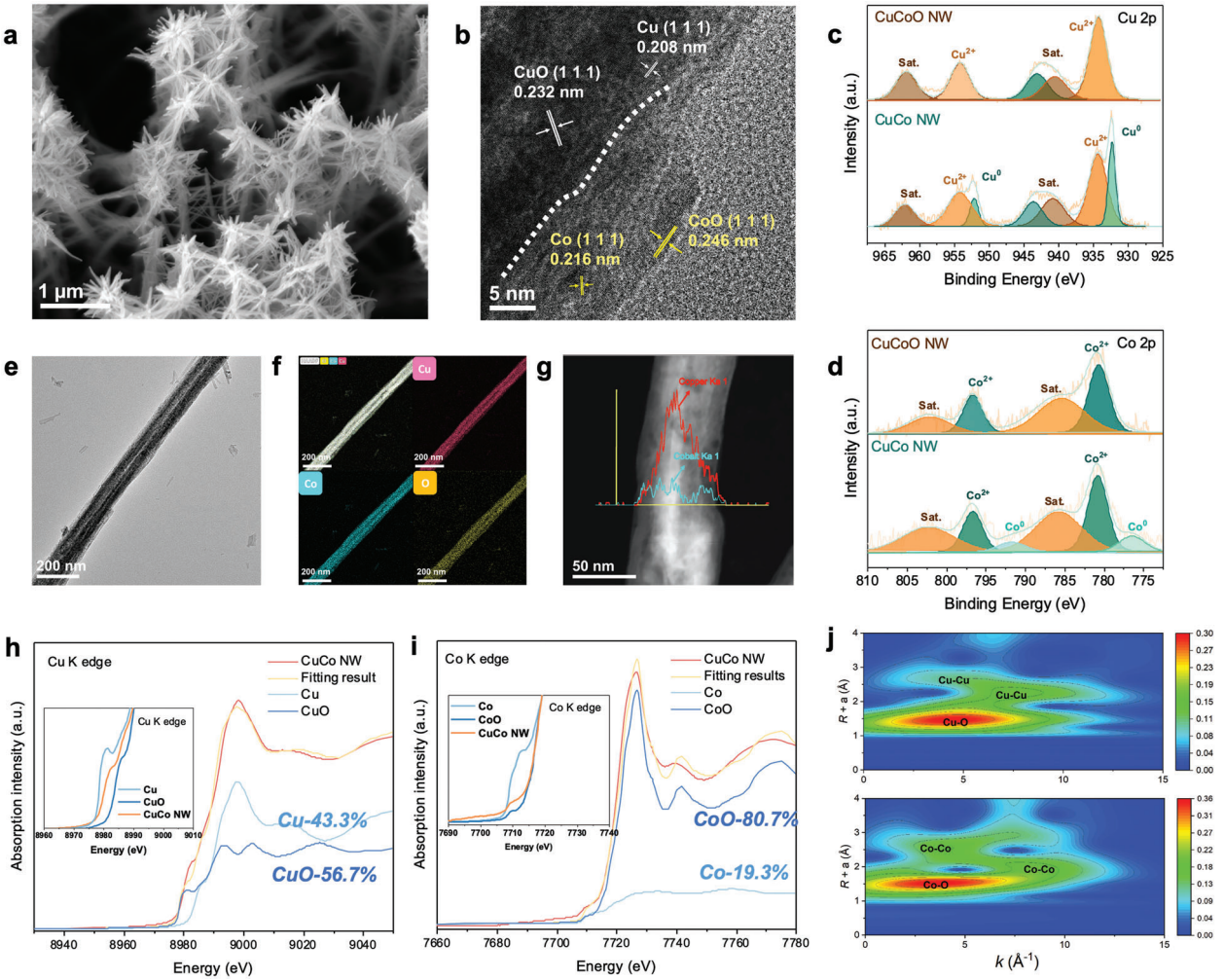

Figure 2. Catalyst characterizations. a) SEM image and b) HRTEM image of CuCo NW. XPS spectra of c) Cu 2p and d) Co 2p of CuCo NW and CuCoO NW. e) TEM image, f) elemental mapping, and g) line-scan spectra of CuCo NW. XANES spectra of h) Cu K edge and i) Co K edge; the insets show the enlargement of the corresponding adsorption edges. j) Wavelet-transform of Cu K edge and Co K edge EXAFS spectra.

Fourier-transformed extended X-ray absorption fine structure spectroscopy (FT-EXAFS) provides detailed information on the coordination structures (Figure S10, Supporting Information). In CuCo NW, the obvious Cu-O peak appears at 1.92 Å while the Cu-Cu peaks appear at 2.36 Å and 2.98 Å. For Co element, Co-O peak appears at 2.08 Å while the Co-Co peaks appear at 2.51 Å and 3.17 Å. In addition, wavelet transform is applied to demonstrate the coordination bond lengths while visually showing the types of coordination atoms (Figure 2j). EXAFS fitting parameters at the Cu K-edge and Co K-edge are presented in detail in Tables S3 and S4 (Supporting Information).

2.2. Electrochemical NO_3RR performance

The electrochemical NO_3RR performance of CuCo NW on Cu foam is investigated under ambient conditions in the static H-cell applying the three-electrode system. Meanwhile, the NO_3RR performance of Cu NW is also investigated as the main control group. As a typical low nitrate concentration for NO_3RR performance evaluation, 2000 ppm of nitrate in 1.0 M KOH is used as the electrolyte here for comparing the intrinsic activity of the catalysts.[7,30] Linear sweep voltammetry (LSV) curves could reveal the activity of the catalysts in NO_3RR intuitively. Meanwhile, the concentration of ammonia, nitrate, and nitrite in the electrolyte is detected through the chromogenic method using UV–vis spectrophotometry. The experimental details are provided in the methods. First, the CuCo NW is tested in 1.0 M KOH with/without nitrate, and the current density under the same potential increases drastically in the presence of nitrate through LSV (Figure S11, Supporting Information). At the potential of −0.3 V versus RHE, the CuCo NW could reach the current density of 600 mA cm^{-2} in the electrolyte with 2000 ppm nitrate, while in the electrolyte without nitrate, this value is only 60 mA cm^{-2} (**Figure 3a**). The huge gap between the two curves suggests that NO_3RR is much more favorable than HER on the CuCo NW. The intrinsic current density is evaluated through j_{ECSA}, suggesting the higher intrinsic activity for CuCo NW in NO_3RR (Figure 3b). Besides, the LSV curves of CuCoO NW, CuO NW and Cu NW are investigated as well (Figure S12, Supporting

© 2024 The Author(s). Advanced Functional Materials published by Wiley-VCH GmbH

16163028, 2024, 44, Downloaded from https://onlinelibrary.wiley.com/doi/10.1002/adfm.202405179 by HONG KONG POLYTECHNIC UNIVERSITY HU NG HOM, Wiley Online Library on [03/11/2024]. See the Terms and Conditions (https://onlinelibrary.wiley.com/terms-and-conditions) on Wiley Online Library for rules of use; OA articles are governed by the applicable Creative Commons License

16163028, 2024, 44, Downloaded from https://onlinelibrary.wiley.com/doi/10.1002/adfm.202405179 by HONG KONG POLYTECHNIC UNIVERSITY HU NG HOM, Wiley Online Library on [03/11/2024]. See the Terms and Conditions (https://onlinelibrary.wiley.com/terms-and-conditions) on Wiley Online Library for rules of use; OA articles are governed by the applicable Creative Commons License

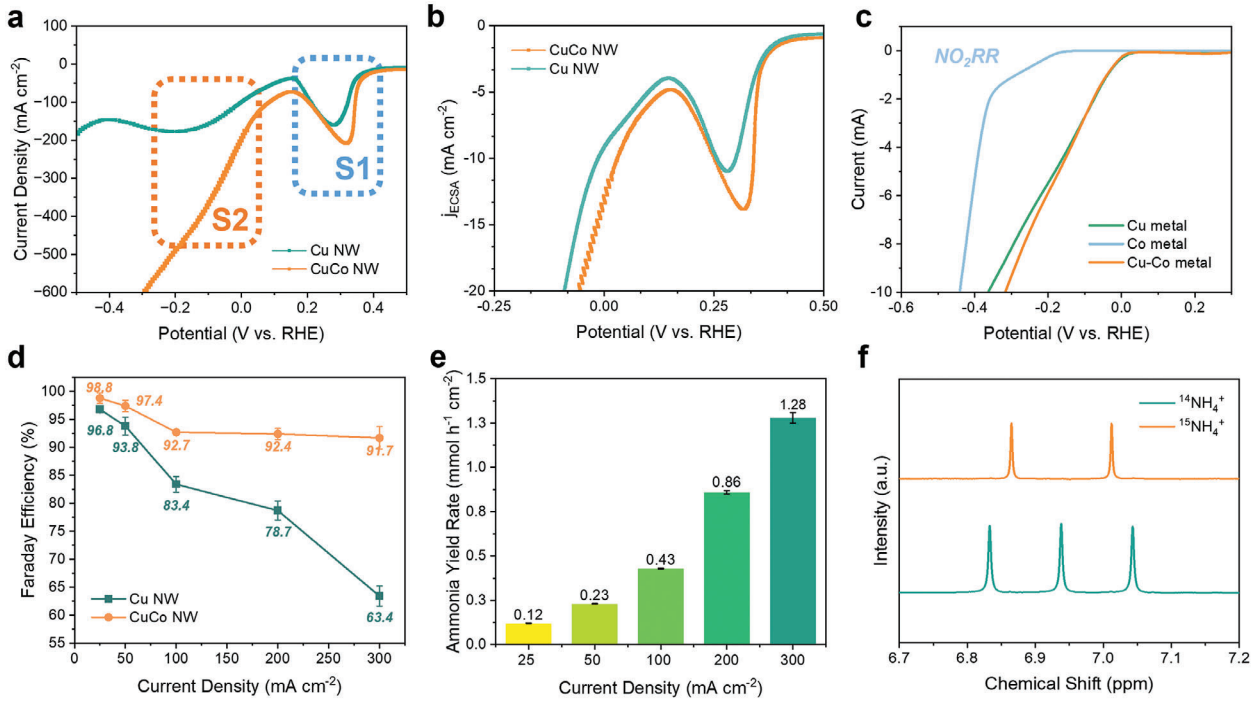

Figure 3. NO_3RR performance in the static H-cell. a) LSV curves of CuCo NW and Cu NW in 1.0 M KOH with 2000 ppm KNO_3 electrolyte. b) J_{ECSA} of CuCo NW and Cu NW. c) RDE LSV curves of pure metal catalysts(Cu, Co, and Cu-Co) at a rotation rate of 1600 rpm in 1.0 M KOH with 2000 ppm KNO_2 electrolyte. d) FE of ammonia production on CuCo NW and Cu NW under different current densities. e) Ammonia yield rate of CuCo NW. f) ^1H NMR spectra of the electrolyte after NO_3RR using $^{15}NO_3^-$ and $^{14}NO_3^-$.

Information). It is clear that catalysts containing metal states show higher NO_3RR activity compared to the corresponding oxidant catalysts. The main control group Cu NW presented distinct electrochemical behaviors compared with CuCo NW. According to the LSV curves, two obvious reduction peaks could be observed, namely S1 and S2[26] Each of the peaks corresponds to one step of the reaction process, and the corresponding equations are given below:[31,32]

$$S1: NO_3^- + H_2O + 2e^- \rightarrow NO_2^- + 2OH^- \quad (2)$$

$$S2: NO_2^- + 5H_2O + 6e^- \rightarrow NH_3 + 7OH^- \quad (3)$$

In the process of NO_3RR, the S1 is the rate-determined step (RDS), and thus the kinetics of NO_3^- to NO_2^- would greatly influence the overall conversion rate to ammonia. Based on the LSV curves, Tafel slopes of CuCo NW and Cu NW were investigated (Figures S13 and S14, Supporting Information). In this range, CuCo NW shows a Tafel slope of 51.47 mV dec^{-1}, which is much smaller than the 97.92 mV dec^{-1} of Cu NW, suggesting rapid S1 kinetics with the addition of Co. Correspondingly, the Tafel slopes of CuCo NW is much smaller in the range of S2 due to the "timely" supplementary of the key intermediate—nitrite. In support of this speculation, commercial metallic Cu, Co, and mixed Cu-Co are investigated separately through rotating disc electrode (RDE) for nitrite reduction (NO_2RR). As shown in Figure 3c, Cu metal shows the leading performance in NO_2RR compared with pure Co metal in RDE. Meanwhile, the performance of mixed Cu–Co metal is close to the Cu metal in NO_2RR indicating that Cu would dominate the S2 process in NO_3RR. The NO_3RR performances of pure metal catalysts through RDE LSV are presented in Figure S15 (Supporting Information) as well, where metallic Cu-Co shows superior electrochemical activity. Combined with the electrochemical impedance spectroscopy, CuCo NW presents a smaller charge transfer impedance, which is merely 0.34 ohm after fitting through the equivalent circuit, highlighting the intrinsic rapid charge transfer kinetics on the electrode-electrolyte surface (Figure S16, Supporting Information). The stability of CuCo NW is examined as well in a H-cell with electrolyte refreshin (Figure S17, Supporting Information).

Ammonia yield is one of the most important aspects of judging the NO_3RR performance. Due to the straightforward relationship between the yield rate and current density, the ammonia production test is carried out under galvanostatic conditions with experimental details in supplementary information (Figures S19–S21, Supporting Information). As shown in Figure 3d, the CuCo NW shows a higher FE of ammonia production than Cu NW under all the current densities chosen in this work. It is notable that with the current density increasing, the gap of the FE between the two samples becomes larger. Under the current density of 300 mA cm^{-2}, the CuCo NW still maintains the FE of 91.7% while the FE for Cu NW is only 63.4%. The result is in accordance with the LSV curves in the former section. Meanwhile, the ammonia yield rate of CuCo NW could reach 1.28 mmol h^{-2} min^{-1} under the current density of 300 mA cm^{-2} (Figure 3e). The continuous conversion from nitrate to ammonia is investigated as well (Figure S18, Supporting Information). During the 120 min NO_3RR process at 200 mA cm^{-2}, almost no N-NO_2 could be detected. Besides,

© 2024 The Author(s). Advanced Functional Materials published by Wiley-VCH GmbH
RIGHTSLINK

the capability of CuCo NW in neutral NO_3RR is also examined, delivering FE of 90.2% at 125 mA cm^{-2} (Figure S22, Supporting Information).

To expel the containments from the environment and avoid false positive results in ammonia production detection, isotope-labeling measurement was adopted in this work using ^1H NMR spectroscopy (Figure 3f). When using the isotope $K^{15}NO_3$ as the nitrogen source, only two peaks could be observed, which confirmed that the ammonia produced and detected in this work is generated from the NO_3RR process rather than the containments from the environment.

2.3. Mechanism Analysis and Theoretical Calculation

Previous electrochemical and ammonia production tests have demonstrated the exceptional activity of the CuCo NW catalyst for selective reduction of NO_3^- to ammonia. The introduction of Co in the catalyst significantly enhances the kinetics of NO_3RR and the FE of ammonia production. To better understand the underlying mechanism of this improvement, we employed in situ characterization techniques and theoretical calculations in this study.

In situ differential electrochemical mass spectrometry (DEMS) is widely used to continuously identify the products and intermediates in Faradic reactions. Not only qualitative but also quantitative, DEMS plays a significant role in the study of the mechanism of electrocatalytic reactions nowadays. Similarly, in situ DEMS was utilized to detect the generated gaseous/volatile intermediates and products/by-products including NH_3, NO, NH_2OH, and H_2 in NO_3RR (**Figure** 4a–d). In addition, the quantitative characteristic enables the cross-sectional comparison between different electrocatalysts under the same reaction conditions. It is obvious that there is an order-of-magnitude difference in the signal intensity of products and intermediates between Cu NW and CuCo NW. For the signals related to NH_3, the CuCo NW presents 100 times higher signal intensity than Cu NW. For the possible intermediates, both the intensities of NO and NH_2OH are ten times larger on CuCo NW, indicating higher ammonia production kinetics on CuCo NW. Meanwhile, the hydrogen signal intensity on Cu NW is higher than that detected on CuCo NW, suggesting the suppression of HER with high NO_3RR activity on CuCo NW. In situ FTIR is employed as well to differentiate the reactive intermediates absorbed on the catalyst electrodes (Figure S23, Supporting Information). The peaks at 1720, 1530, 1250, and 1110 cm^{-1} are associated with absorbed NH_3, NH_2, NO_2^- and NH_2OH, respectively[33] To be mentioned, the peak for NO_3^- cannot be found due to the rapid consumption and low concentration suggesting the rapid kinetics of the nitrite generation step. Combining the detected intermediates and previously reported NO_3RR routes, it can be deduced that the NO_3RR could be broken down into a series of deoxygenation/hydrogenation steps and final desorption of ammonia.

Besides, In situ Raman spectroscopy is a powerful method for the identification of active species due to the unlimited pressure, temperature, or the presence of reaction gases during the measurement process. To derive the active phases during the NO_3RR process, in situ Raman was used to monitor the phase evolution of CuCo NW in the electrolyte of 1.0 M KOH and 2000 ppm KNO_3 at a series of applied potential from 0.4 to −0.2 V versus RHE (Figure 4e). Interestingly, when the potential becomes negative (lower than 0.0 V vs RHE), the peaks for CuO and CoO disappear, indicating the surface of the catalyst is reduced to metallic Cu and Co during the process. However, the catalyst could remain high FE for ammonia at 300 mA cm^{-2} (corresponding to 0.0 V vs RHE) and even higher current density in the flow system, which sheds light on the metallic phases (Cu and Co) as active sites.

A density functional theory (DFT) calculation is conducted to elucidate the mechanism responsible for the enhanced NO_3RR performance resulting from the introduction of the Co phase. Utilizing the prior experimental characterization, Cu (111) and Co (111) surfaces were selected as the model's active planes, and the reaction pathway is as follows: $*NO_3 \rightarrow *NO_3H \rightarrow *NO_2 \rightarrow *NO_2H \rightarrow *NO \rightarrow *NOH \rightarrow *NHOH \rightarrow *NH_2OH \rightarrow *NH_2 \rightarrow *NH_3$[11]. To initiate the analysis, separate free energy diagrams of NO_3RR on Cu (111) and Co (111) surfaces were computed at a fixed potential of −0.2 V versus RHE at a pH of 14 (refer to computational details in Supporting Information). Figure 4f illustrates the schematic of the NO_3RR process with intermediate structures on Cu (111) and Co (111), while Figure 4g depicts the associated free energy diagram. Of particular interest is the deoxygenation step from NO_3^- to NO_2, where Cu (111) and Co (111) exhibit distinct activities. Initially, NO_3^- is more strongly adsorbed on Co (111), with a free energy change (ΔG) of −0.005 eV from NO_3^- to $*NO_3$, while for Cu (111) this step is endothermic with ΔG of 0.029 eV. A more significant difference is observed in the deoxygenation process from $*NO_3$ to $*NO_2$, as shown in Figure 4f. On the Cu (111) surface, this process generates $*NO_3H$ as the intermediate, involving an uphill ΔG of 0.694 eV. This step serves as the rate-determining step (RDS) of NO_3RR on Cu (111), aligning with previous theoretical computations[14] Conversely, on the Co (111) surface, the adsorbed $*NO_3H$ spontaneously dissociates into adsorbed $*NO_2$ and *OH (Figure 4f, in the dashed box). This step is exothermic, with a ΔG of −1.878 eV. The computational results strongly suggest that Co (111) is more active for NO_3^- reduction to NO_2 and dominates the initial steps of NO_3RR. However, in the subsequent step from $*NO_2$ to $*NO_2H$, it serves as the RDS of NO_3RR for Co (111). The ΔG for this step is 0.428 eV, which is greater than that of Cu (111) (ΔG = 0.324 eV). Consequently, we infer that Co (111) and Cu (111) can form a tandem catalytic pathway, where $*NO_3$ is initially absorbed on Co (111) and deoxygenated to form $*NO_2$. Subsequently, $*NO_2$ is transferred to Cu (111) and further converted to $*NH_3$, thereby reducing the ΔG of the RDS of the individual surfaces and establishing an optimal pathway, as summarized in the inset figure of Figure 4g. The ΔG of the RDS of tandem route is reduced to 0.324 eV compared with the values of individual Co (111) (0.428 eV) and Cu (111) (0.694 eV).

To validate the tandem mechanism, the efficient migration of the key intermediate $*NO_2$ on the Co (111) and Cu (111) becomes crucial. The migration of NO_2 on the surface was investigated using the climbing-image nudged elastic band method. The calculated minimum energy path of NO_2 migration on pure Co (111), Cu (111), and the interface of Co (111) and Cu (111) is shown in Figure 4g. The migration energy barriers (E_b) on the pure Co (111) and Cu (111) surfaces are 0.180 and 0.250 eV, respectively, as illustrated in Figure S37 (Supporting Information). This indicates that the migration of NO_2 on the surfaces of both materials

© 2024 The Author(s). Advanced Functional Materials published by Wiley-VCH GmbH
RIGHTSLINK

16163028, 2024, 44, Downloaded from https://onlinelibrary.wiley.com/doi/10.1002/adfm.202405179 by HONG KONG POLYTECHNIC UNIVERSITY HU NG HOM, Wiley Online Library on [03/11/2024]. See the Terms and Conditions (https://onlinelibrary.wiley.com/terms-and-conditions) on Wiley Online Library for rules of use; OA articles are governed by the applicable Creative Commons License

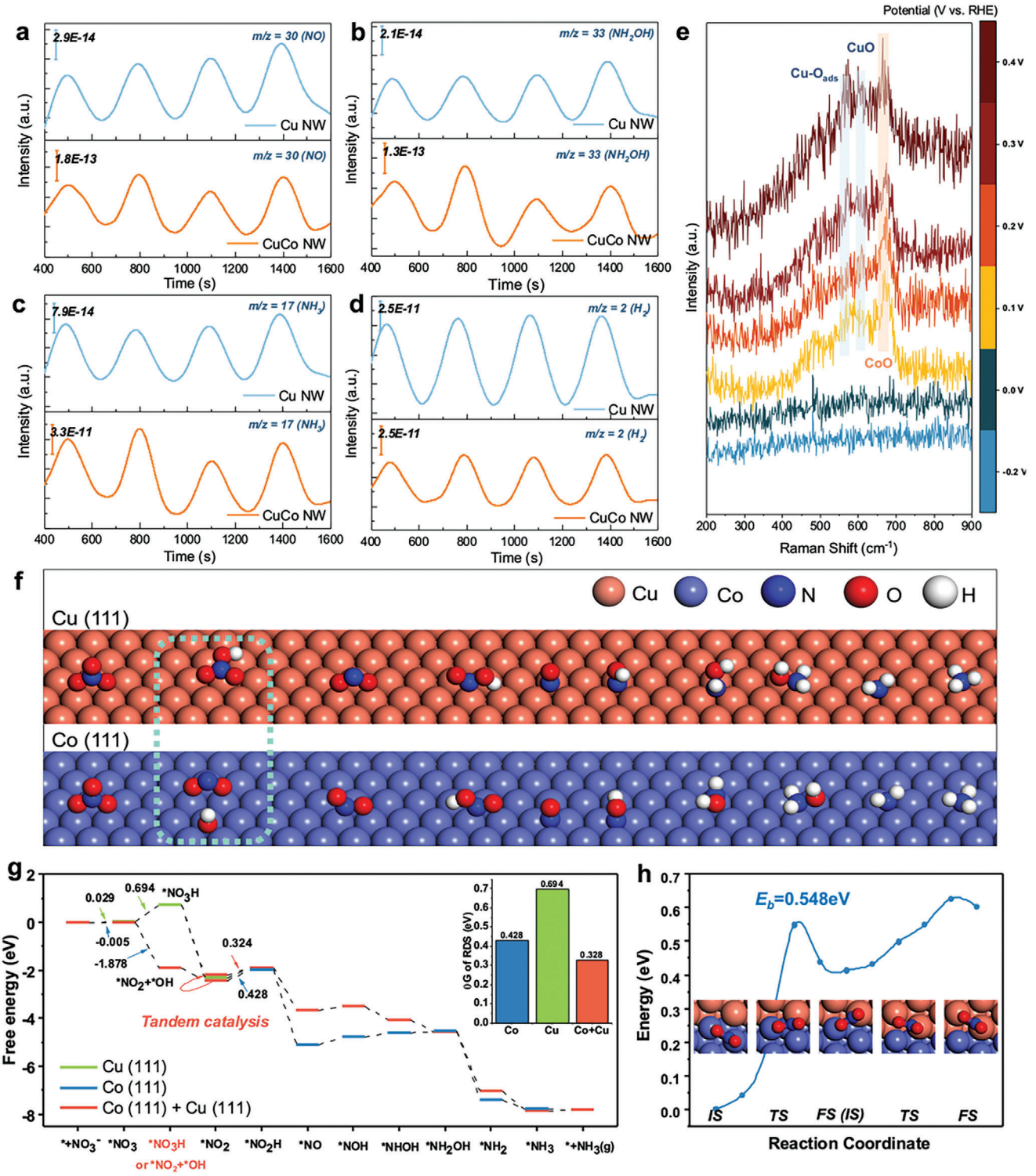

Figure 4. Mechanism insights. In situ DEMS spectra of a) NH_3, b) NO, c) NH_2OH, and d) H_2 detected during cyclic voltammetry in the potential range of 0.4 to −0.4 V on Cu NW and CuCo NW. e) In situ Raman spectra in the potential range of 0.4 to −0.2 V on CuCo. DFT calculations of f) NO_3RR intermediates on Cu (111) and Co (111). g) Calculated Gibbs free energy changes (DG) of NO_3RR over Cu (111), Co (111), and the tandem route (Co (111) + Cu (111)) at a fixed potential of −0.2 V versus RHE at pH of 14. The inset figure summarizes the DG of the RDS of NO_3RR over Cu (111), Co (111) and tandem route. h) Calculated minimum energy path of NO_2 migration at the interface of Co (111) and Cu (111). The inset maps are the regional configurations of initial state (IS), transition state (TS), and final state (FS) in the migration.

© 2024 The Author(s). Advanced Functional Materials published by Wiley-VCH GmbH

RIGHTSLINK

16163028, 2024, 44, Downloaded from https://onlinelibrary.wiley.com/doi/10.1002/adfm.202405179 by HONG KONG POLYTECHNIC UNIVERSITY HU NG HOM, Wiley Online Library on [03/11/2024]. See the Terms and Conditions (https://onlinelibrary.wiley.com/terms-and-conditions) on Wiley Online Library for rules of use; OA articles are governed by the applicable Creative Commons License

is highly rapid. Furthermore, the E_b for NO_2 migration on the interface of Co (111) and Cu (111) is 0.548 eV, suggesting the kinetic feasibility of NO_2 migration from Co (111) to Cu (111) at room temperature, as depicted in Figure 4g. It is noteworthy that, according to Eyring equation, reactions with activation barrier <0.900 eV can occur at room temperature (see computational details in Supporting Information).

In addition, considering the competitive side reaction of NO_3RR, the HER is examined on Cu (111) and Co (111) surfaces. Under alkaline conditions, protons for the HER reaction are obtained from the dissociation of water molecules. We calculated the free energy diagram of HER process at a fixed potential of −0.2 V versus RHE at a pH of 14. As illustrated in Figure S36 (Supporting Information), water adsorption is the RDS for HER on both Cu (111) and Co (111) surfaces, with ΔG values of 0.459 and 0.611 eV, respectively. These values are higher than the ΔG of the RDS involved in NO_3RR (0.324 eV) through the tandem route. These results establish that the catalyst can effectively inhibit the competition of the HER.

The computational findings are supported by previous RDE experimental results (Figure 3a; Figure S15, Supporting Information). When nitrate is used as the reactant, the Cu-Co nanoparticles demonstrate a significant advantage over both the Cu and Co nanoparticles. In order to simulate the step from $*NO_2$ to $*NH_3$ in the NO_3RR process, nitrite is selected as the reactant in the RDE test (Figure 3a). As previously mentioned, the Cu-Co nanoparticles exhibit the best NO_2RR electrochemical performance, while the pure Cu nanoparticles show a similar performance. This suggests a preference for $*NO_2$ to $*NH_3$ on the Cu metal surface, indicating the optimal pathway by reducing the ΔG of the RDS of the individual surfaces.

Incorporating both experimental and computational data, the introduction of Co (111) instigates tandem catalysis when paired with Cu (111). The stronger adsorption of NO_3^- on Co (111) and the resulting exothermic change in the pathway from $*NO_3$ to $*NO_2$ highlights the superior activity of Co (111) in the initial stages of NO_3RR. However, the subsequent transition from $*NO_2$ to $*NO_2H$, identified as the RDS for Co (111), is more favorable on Cu (111). Additionally, the high rate of $*NO_2$ migration between Co (111) and Cu (111) suggests the kinetic feasibility of this tandem catalysis. In this way, an optimal tandem pathway for NO_3RR is established through reducing the ΔG of the RDS on individual surfaces, offering valuable insights for future catalyst design and emphasizing the potential of tandem catalysis in enhancing NO_3RR performance.

2.4. Reactor Development and Ammonia Mass-Production

With the impressive intrinsic catalytic activity for NO_3RR to ammonia, the practical application of as-prepared CuCo NW is demonstrated through the development of a flow reactor. Compared with a static H-cell reactor (Figure S24, Supporting Information) the flow reactor greatly enhances the mass transfer for the reactants and products, providing stable conditions (e.g., concentration, pH value, etc.) for the reaction. Specifically, integrated CuCo NW/Cu foam is utilized as the cathode and commercial Ni foam is chosen as the anode. An anion exchange membrane (AEM) is utilized to separate the catholyte and anolyte, preventing the oxidation of NH_3 on the anode, as depicted in **Figure 5a**. The schematic of the flow reactor components and the setup is shown in Figures S25 and S26 (Supporting Information). In this flow system, the electrolytes are fed into the flow cell through two peristaltic pumps. The anolyte is 1.0 M KOH to improve the conductivity. The catholyte is 1.0 M KOH and KNO_3 at a certain concentration. Due to the porous structure of Cu foam and the branched-nanowire structure of CuCo NW, the nitrate ions diffuse into the cathode after passing through the interface between the flow channel and electrode. Then, the NO_3RR would proceed on the surface of the cathode, converting NO_3^- into NH_3 in the alkaline condition, while coupling oxygen evolution reaction (OER) on the anode. The electrochemical equations of this reactor for ammonia production are presented below:

$$\text{Cathode}: \quad NO_3^- + 6H_2O + 8e^- \rightarrow NH_3 + 9OH^- \qquad E^0 = 0.69 \text{ V vs. RHE} \tag{4}$$

$$\text{Anode}: \quad 8OH^- \rightarrow 2O_2 + 4H_2O + 8e^- \qquad E^0 = 1.23 \text{ V vs. RHE} \tag{5}$$

$$\text{Overall}: \quad NO_3^- + 2H_2O \rightarrow 2O_2 + NH_3 + OH^- \qquad U^0 = 0.54 \text{ V} \tag{6}$$

The stability of the flow system is the prerequisite for the practical application, which is determined by the stability of the individual components, such as catalyst, working conditions, cell components, etc.[34] Thus, we conducted the long-term operation test at the current density of 100 and 200 mA cm^{-2}. As shown in Figure 5b, the flow reactor maintains the ammonia FE for over 90% after 200 h-operation with stable voltage. The stability of CuCo NW/Cu foam cathode is also examined directly through material characterization and electrochemical characterization of the electrode after the 200 h operation period. After the long-term stability test, the nanowire structure is largely preserved as shown in SEM image (Figure S27, Supporting Information), while the XPS spectra indicate the stability of chemical composition of CuCo NW (Figures S28 and S29, Supporting Information). The EIS spectra after long term stability test are investigated as well (Figure S30, Supporting Information). It could be found out that after the 200 h operation, the R_{ct} of CuCo NW/Cu foam slightly increased to 0.37 ohm while it is still much smaller than the 0.50 ohm of Cu NW/Cu foam. The LSV curve and EIS spectra of the flow reactor in 2000 ppm NO_3^- are also investigated (Figure S31, Supporting Information). Besides, the FE and ammonia yield rates under different current densities are investigated (Figure 5c). It is not surprising to find out that in the flow system, with enhanced mass transfer of nitrate, the ammonia selectivity would further increase in the 2000 ppm NO_3^- and realize the FE of 93.8% at 600 mA cm^{-2}. Moreover, the flow cell system enables the ampere-level current density, where the ammonia yield rate could reach up to 3.07 mmol h^{-1} cm^{-2}.To study the effect of nitrate concentration on ammonia production, the higher concentration of NO_3^- is applied in this flow reactor. With the increase of nitrate concentration to 0.1 and 0.3 M in catholyte, the FE and ammonia yield rate would increase respectively. As shown in Figure 5d, in the 1.0 M KOH and 0.3 M KNO_3, the FE could reach 90.1% under 1.0 A cm^{-2} and maintain 74.4% at the current density of 3.0 A cm^{-2}. Meanwhile, the ammonia yield rate could reach the astonishing 10.41 mmol h^{-1} cm^{-2} at 3.0 A cm^{-2},

© 2024 The Author(s). Advanced Functional Materials published by Wiley-VCH GmbH
RIGHTSLINK
16163028, 2024, 44, Downloaded from https://onlinelibrary.wiley.com/doi/10.1002/adfm.202405179 by HONG KONG POLYTECHNIC UNIVERSITY HU NG HOM, Wiley Online Library on [03/11/2024]. See the Terms and Conditions (https://onlinelibrary.wiley.com/terms-and-conditions) on Wiley Online Library for rules of use; OA articles are governed by the applicable Creative Commons License

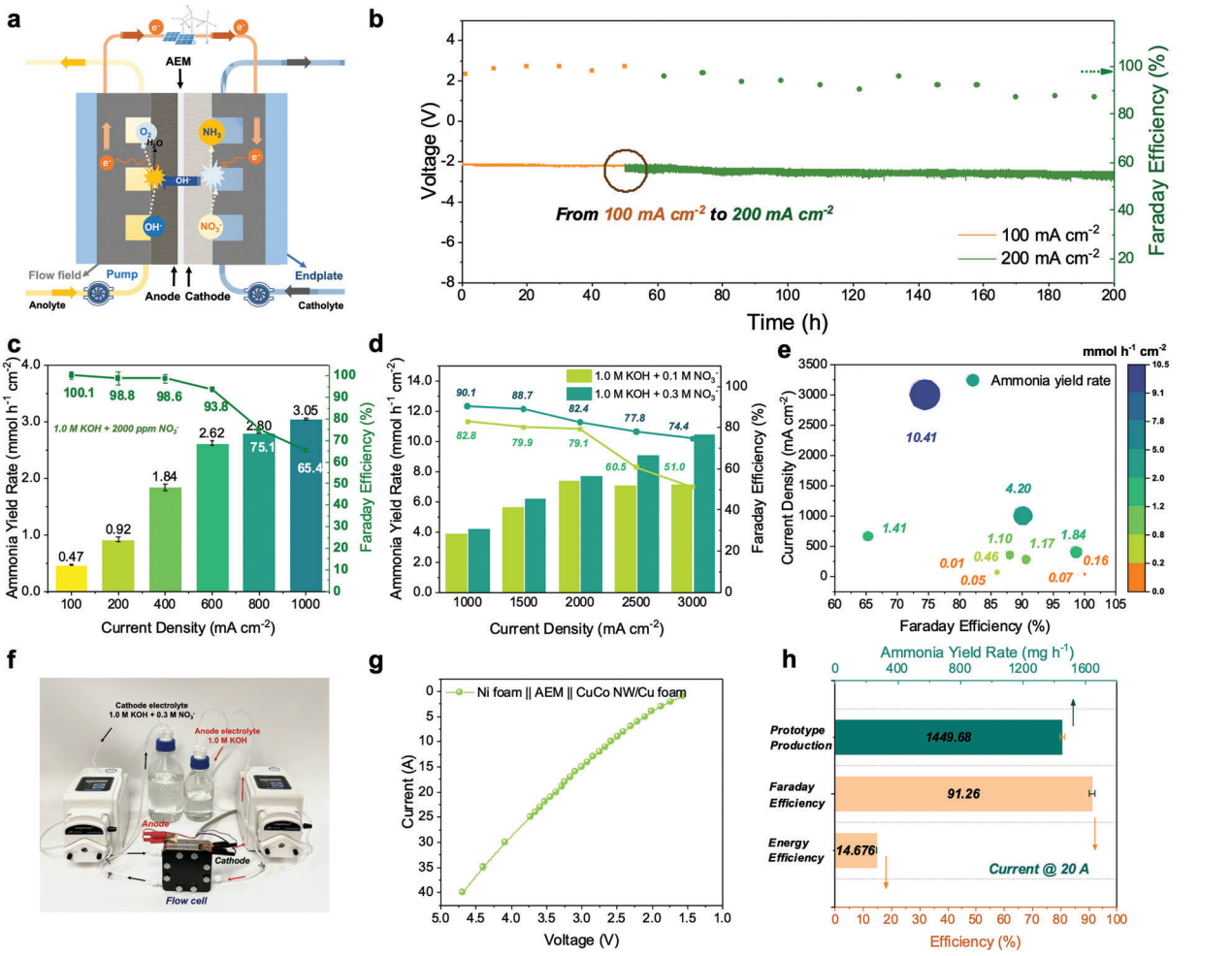

Figure 5. Continuous production of ammonia in a flow reactor. a) Schematic illustration of the working principle for the flow reactor. b) Time-dependent current density and FE of ammonia in 200 h long-term operation. c) Ammonia yield rate and FE in a flow reactor. d) The influence of nitrate concentration on FE and ammonia yield rate at high current densities. e) Comparison of ammonia production performance with previously reported works. f) Experimental setup and g) *I–V* curve of the scaling-up prototype (active area: 20.0 cm^2). h) Production of ammonia, FE, and EE at 20 A in the scaling-up prototype.

which is one of the highest ammonia yield rates per unit area reported to date (Figure 5e; Table S7, Supporting Information).

Aiming at the mass production of ammonia through electrochemical nitrate conversion, a scaling-up prototype with a 20-times larger active area (20.0 cm^2) is fabricated (Figure S32, Supporting Information). The experimental setup is presented in Figure 5f, which enables the current up to tens of amperes level for a single cell. The *I–V* curve of the scaling-up prototype is shown in Figure 5g. With the compact design, the solution resistance (R_s) of the prototype is 0.06 ohm according to EIS spectra (Figure S33, Supporting Information). Notably, the ammonia production performance was evaluated at a series of current density from 2.0 to 20.0 A, which are among the highest recorded level of current for NO_3RR (Figure S34, Supporting Information). In Figure 5h, it is surprising to find out that the FE could maintain 91.26% with the ammonia yield rate of 1474.09 mg h^{-1} (equivalent to 35.38 g day^{-1}), fulfilling the electrochemical mass production of ammonia. Furthermore, the long-term operation at 20.0 A is inspected and enables stable operation for over 10 h (Figure S35, Supporting Information). The energy efficiency of this prototype is investigated as well in this work. However, the value of 14.68% at 20.0 A still has room for improvement. In future, the anode reaction and working conditions of the scaling-up reactor deserve further investigation.

Overall, we have demonstrated great potential in the practical application of electrochemical ammonia production and fabricated the prototype to fulfill the mass production using our CuCo NW catalyst.

3. Conclusion

In summary, we reported a tandem catalysis mechanism on metallic Co and Cu, of which Co (111) preferentially adsorbed NO_3^- and converted into NO_2^-, then Cu (111) sequent converted NO_2^- into NH_3 through steps of deoxygenation and hydrogenation. As suggested by in situ electrochemical tests and DFT calculations, this contributes to the excellent NO_3RR performance

© 2024 The Author(s). Advanced Functional Materials published by Wiley-VCH GmbH

16163028, 2024, 44, Downloaded from https://onlinelibrary.wiley.com/doi/10.1002/adfm.202405179 by HONG KONG POLYTECHNIC UNIVERSITY HU NG HOM, Wiley Online Library on [03/11/2024]. See the Terms and Conditions (https://onlinelibrary.wiley.com/terms-and-conditions) on Wiley Online Library for rules of use; OA articles are governed by the applicable Creative Commons License

of our synthesized CuCo NW catalyst by optimizing the energy pathway. In a flow reactor, the CuCo NW could realize the FE of 93.8% at 600 mA cm^{-2} in a low nitrate concentration of 2000 ppm (0.032 M). With a higher nitrate concentration of 0.3 M, ammonia production of CuCo NW could reach FE of 90.13% at 1.0 A cm^{-2} and yield rate of 10.41 mmol h^{-1} cm^{-2} at 3.0 A cm^{-2}. Moreover, aiming at practical ammonia production, a scaling-up prototype is fabricated and finally realizes the ammonia yield rate of 1474.09 mg h^{-1} and FE of 91.26% at 20.0 A. In conclusion, this work not only presents an efficient tandem catalysis mechanism for NO_3RR but also maps out its great potential for industrial mass production.

Supporting Information

Supporting Information is available from the Wiley Online Library or from the author.

Acknowledgements

The authors acknowledge the support from the National Natural Science Foundation of China (No. 22205187, No. 22209061), the Hong Kong Polytechnic University (CD4D and WZ4Q), and a grant from the Research Institute for Smart Energy (CDA4) at the Hong Kong Polytechnic University, and the Start-up Fund for Senior Talents in the Jiangsu University (21JDG060).

Conflict of Interest

The authors declare no conflict of interest.

Author Contributions

L.A. and X.Z. proposed the topic. K.Z. designed and conducted the experiment and drafted the manuscript. P.S., Z.S., and Y.W. conducted the theoretical calculation. Y.H. and C.L. conducted the X-ray absorption spectroscopy experiment and analysis. All authors contributed to the editing of the manuscript.

Data Availability Statement

The data that support the findings of this study are available from the corresponding author upon reasonable request.

Keywords

electrocatalyst, nitrate reduction, tandem catalysis

Received: March 26, 2024
Revised: May 10, 2024
Published online: May 27, 2024

[1] X. Cui, C. Tang, Q. Zhang, *Adv. Energy Mater.* **2018**, *8*, 1800369.
[2] S. L. Foster, S. I. P. Bakovic, R. D. Duda, S. Maheshwari, R. D. Milton, S. D. Minteer, M. J. Janik, J. N. Renner, L. F. Greenlee, *Nat. Catal.* **2018**, *1*, 490.
[3] V. Kyriakou, I. Garagounis, E. Vasileiou, A. Vourros, M. Stoukides, *Catal. Today* **2017**, *286*, 2.
[4] B. H. Suryanto, H.-L. Du, D. Wang, J. Chen, A. N. Simonov, D. R. MacFarlane, *Nat. Catal.* **2019**, *2*, 290.
[5] D. Xu, Y. Li, L. Yin, Y. Ji, J. Niu, Y. Yu, *Front. Environ. Sci. Eng.* **2018**, *12*, 1.
[6] Y. Fernández-Nava, E. Maranon, J. Soons, L. Castrillón, *Bioresour. Technol.* **2008**, *99*, 7976.
[7] F. Chen, Z. Wu, S. Gupta, D. J. Rivera, S. V. Lambeets, S. Pecaut, J. Y. T. Kim, P. Zhu, Y. Z. Finfrock, D. M. Meira, *Nat. Nanotechnol.* **2022**, *17*, 1.
[8] S. Garcia-Segura, M. Lanzarini-Lopes, K. Hristovski, P. Westerhoff, *Appl. Catal., B* **2018**, *236*, 546.
[9] Z. Wang, D. Richards, N. Singh, *Catal. Sci. Technol.* **2021**, *11*, 705.
[10] M. Karamad, T. J. Goncalves, S. J. Villegas, I. Gates, S. Siahrostami, *Faraday Discuss.* **2022**, *243*, 502.
[11] Y. Fu, S. Wang, Y. Wang, P. Wei, J. Shao, T. Liu, G. Wang, X. Bao, *Angew. Chem., Int. Ed.* **2023**, *62*, 202303327.
[12] J. Zhao, L. Liu, Y. Yang, D. Liu, X. Peng, S. Liang, L. Jiang, *ACS Sustainable Chem. Eng.* **2023**, *11*, 2468.
[13] J. Liu, D. Richards, N. Singh, B. R. Goldsmith, *ACS Catal.* **2019**, *9*, 7052.
[14] M. Wei, S. Li, X. Wang, G. Zuo, H. Wang, X. Meng, J. Wang, *Adv. Energy Sustain. Res.* **2023**, *5*, 2300173.
[15] H. Liu, J. Li, F. Du, L. Yang, S. Huang, J. Gao, C. Li, C. Guo, *Green Energy Environ.* **2023**, *8*, 1619.
[16] Y. Wang, A. Xu, Z. Wang, L. Huang, J. Li, F. Li, J. Wicks, M. Luo, D.-H. Nam, C.-S. Tan, *J. Am. Chem. Soc.* **2020**, *142*, 5702.
[17] W. He, J. Zhang, S. Dieckhöfer, S. Varhade, A. C. Brix, A. Lielpetere, S. Seisel, J. R. Junqueira, W. Schuhmann, *Nat. Commun.* **2022**, *13*, 1129.
[18] S. Chen, K. Lian, W. Liu, Q. Liu, G. Qi, J. Luo, X. Liu, *Nano Res.* **2023**, *16*, 9214.
[19] M. Yang, G. Meng, H. Li, T. Wei, Q. Liu, J. He, L. Feng, X. Sun, X. Liu, *J. Colloid Interface Sci.* **2023**, *652*, 155.
[20] S. Chen, G. Qi, R. Yin, Q. Liu, L. Feng, X. Feng, G. Hu, J. Luo, X. Liu, W. Liu, *Nanoscale* **2023**, *15*, 19577.
[21] K. Chen, J. Xiang, Y. Guo, X. Liu, X. Li, K. Chu, *Nano Lett.* **2024**, *24*, 541.
[22] S. Wang, V. Petzold, V. Tripkovic, J. Kleis, J. G. Howalt, E. Skulason, E. Fernández, B. Hvolbæk, G. Jones, A. Toftelund, *Phys. Chem. Chem. Phys.* **2011**, *13*, 20760.
[23] F. Li, Y. C. Li, Z. Wang, J. Li, D.-H. Nam, Y. Lum, M. Luo, X. Wang, A. Ozden, S.-F. Hung, *Nat. Catal.* **2020**, *3*, 75.
[24] R. D. Milton, S. D. Minteer, *ChemPlusChem* **2017**, *82*, 513.
[25] X. Zhang, X. Liu, Z.-F. Huang, L. Guo, L. Gan, S. Zhang, M. Ajmal, L. Pan, C. Shi, X. Zhang, *ACS Catal.* **2023**, *13*, 14670.
[26] J. Fang, Q. Zheng, Y. Lou, K. Zhao, S. Hu, G. Li, O. Akdim, X. Huang, S. Sun, *Nat. Commun.* **2022**, *13*, 7899.
[27] Y. Hsu, Y. Chen, Y. Lin, *J. Electroanal. Chem.* **2012**, *673*, 43.
[28] R. Sundaresan, V. Mariyappan, T.-W. Chen, S.-M. Chen, N. Karuppusamy, M. Akilarasan, *Int. J. Electrochem. Sci.* **2021**, *16*, 210829.
[29] G. Carson, M. Nassir, M. Langell, *J. Vac. Sci. Technol., A* **1996**, *14*, 1637.
[30] M. B. Hariri, G. G. Botte, *J. Electrochem. Soc.* **2023**, *170*, 053502.
[31] V. Rosca, M. Duca, M. T. de Groot, M. T. Koper, *Chem. Rev.* **2009**, *109*, 2209.
[32] D. Reyter, D. Bélanger, L. Roué, *Electrochim. Acta* **2008**, *53*, 5977.
[33] S. Han, H. Li, T. Li, F. Chen, R. Yang, Y. Yu, B. Zhang, *Nat. Catal.* **2023**, *6*, 402.
[34] E. Kolle-Görgen, G. Fortunato, M. Ledendecker, *Chem. Mater.* **2022**, *34*, 10223.

© 2024 The Author(s). Advanced Functional Materials published by Wiley-VCH GmbH

RIGHTSLINK

16163028, 2024, 44, Downloaded from https://onlinelibrary.wiley.com/doi/10.1002/adfm.202405179 by HONG KONG POLYTECHNIC UNIVERSITY HU NG HOM, Wiley Online Library on [03/11/2024]. See the Terms and Conditions (https://onlinelibrary.wiley.com/terms-and-conditions) on Wiley Online Library for rules of use; OA articles are governed by the applicable Creative Commons License